

Combining Geometric and Topological Information in Image Segmentation

Hengrui Luo

Department of Statistics, The Ohio State University

Justin Strait

Department of Statistics, University of Georgia

Abhijoy Saha

Department of Statistics, The Ohio State University

April 15, 2021

Abstract

A fundamental problem in computer vision is image segmentation, where the goal is to delineate the boundary of the object in the image. The focus of this work is on the segmentation of grayscale images and its purpose is two-fold. First, we conduct an in-depth study comparing active contour and topologically-based methods, two popular approaches for boundary detection of 2-dimensional images. Certain properties of the image dataset may favor one method over the other, both from an interpretability perspective as well as through evaluation of performance measures. Second, we propose the use of topological knowledge to assist an active contour method, which can potentially incorporate prior shape information. The latter is known to be extremely sensitive to algorithm initialization, and thus, we use a topological model to provide an automatic initialization. In addition, our proposed model can handle objects in images with more complex topological structures. We demonstrate this on artificially-constructed image datasets from computer vision, as well as real medical image data.

Keywords: Image segmentation, active contours, topological data analysis, shape analysis.

1 Introduction

1.1 The Segmentation Problem

The motivation of this paper is to study how geometric and topological information can be used together to improve existing methods in a specific, well-defined image analysis problem. Image segmentation refers to methods which delineate the contour (or boundary) of objects within an image. This important problem has been extensively studied in engineering, computer science, and statistics literature (Huang & Dom, 1995; Zhang, 1996; Arbelaez *et al.*, 2011; Bryner *et al.*, 2013). Classical statistical shape analysis methods (Kendall, 1989) and recently developed topological methods (Carlsson, 2009) can both be applied to this problem. One of the advantages of a statistical approach to the segmentation problem is that it provides an explicit model for the underlying image; therefore formal inference can be carried out.

Intuitively, the topology and shape of the object is important information which should help guide segmentation. However, it is not completely clear at the moment on which datasets statistical shape analysis methods (Kendall, 1989; Joshi & Srivastava, 2009; Bryner *et al.*, 2013) and topologically-based methods (Paris & Durand, 2007; Carlsson, 2009; Ghrist, 2014) can both be applied. Data-generating mechanisms are important for shape analysis, while topologically-based methods usually consider a (static) point set at different scales, without specific consideration on its data-generating mechanisms.

In a broader sense, this paper is also an attempt to answer the open problem of comparing statistical procedures and topological data analysis (TDA) using this very concrete segmentation problem, as asked by Wasserman (2018). The difficulty in conducting such a comparison is that in most statistical problems where TDA can be applied, there is not a precise measurement of performance. Conversely, for some well-formulated statistical problems, TDA does not see a direct application. We discover that the image segmentation problem we will describe is a carefully crafted problem where both TDA and shape analysis will find natural applications.

One perspective to image segmentation is to treat it as a *point clustering problem*. Arbelaez *et al.* (2011) present a unified approach to the 2-dimensional image segmentation problem and an exhaustive comparison between their proposed global-local methods with existing classical methods based on the Berkeley Segmentation Dataset (BSDS300). Following their insights, the image segmentation problem can be formulated as an unsupervised clustering problem of feature points. For a 2-dimensional grayscale image, the dataset comes in the form of pixel positions (x_i, y_i) representing the 2-dimensional coordinates, and the density function value f_i , evaluated at the same position representing *grayscale values* $g_i \in [0, 1]$ at that particular pixel location. The term *feature space* is used to describe the product space of the position space and scale density

space, whose coordinates are $((x_i, y_i), f_i)$. For a grayscale image, the feature space is $\mathbb{R}^2 \times \mathbb{R}^1$ and the feature points $((x_i, y_i), g_i)$ will be clustered according to some criteria, usually related to the density value f_i . Considering a pixel image as a dataset consisting of n feature points, we can view the segmentation problem as a clustering problem. The most straightforward way to cluster pixel points is according to their density value f_i . This naive clustering method works well when the image is binary and without any noise, i.e. $f_i \in \{0, 1\}$. One can also cluster these points according to their limit points under kernel weighted averages, as shown in Paris & Durand (2007). Finer criteria of clustering usually lead to better performance for a broader class of images. The final result is a clustering of pixel points, equivalent to grouping the points according to some criterion (e.g., their corresponding density modal sets in the binary case). As pointed out by Paris & Durand (2007), hierarchical clustering structure is intrinsically related to multi-scale analysis, which can be studied by looking at level sets of pixel density functions.

A different perspective to the image segmentation problem is to treat it as a *curve estimation problem*, as described in the active contour literature (Caselles *et al.*, 1997; Joshi & Srivastava, 2009; Bryner *et al.*, 2013; Bryner & Srivastava, 2014). In this setting, the goal is to estimate the boundaries of objects found in images. In other words, the output is a curve in \mathbb{R}^2 , which separates a targeted object of interest from the image background. In this approach, the boundary curve is estimated by minimizing an energy functional defined by image and auxiliary terms (Joshi & Srivastava, 2009; Bryner *et al.*, 2013). One of the most influential papers in this area is Kass *et al.* (1988), referring to active contour models as “snakes.” A typical energy functional is comprised of two terms: one term uses pixel value information both inside and outside the current curve iteration to “push” regions of the curve towards important features in an image. The other term tries to balance this energy with an inherent desire for smooth object boundaries. Following this line of research, Zhu & Yuille (1996) developed the region competition approach, and Caselles *et al.* (1997) derived a different method also based on the idea of active contours. In this paper, we adopt the Bayesian active contour approach proposed by Joshi & Srivastava (2009) and adapted by Bryner *et al.* (2013), which includes an additional term incorporating prior shape information about the object of interest.

1.2 Topological Data Analysis

Topological data analysis (TDA) has witnessed rapid growth in the past decades. Besides the physical application of characterizing crystal structure (Hiraoka *et al.*, 2016) and astronomical study of cosmic webs (Van de Weygaert *et al.*, 2011), researchers use topological summaries (e.g., persistence diagrams) in scenarios such as protein flexibility measurement (Xia & Guo, 2014; Gameiro *et al.*, 2015). These applications make use of the topological summary as a new characterization

of the data, which has the potential into provide additional insight to data analysis.

An essential line of application research focuses on the hierarchical clustering structure provided by TDA techniques and is applied to image processing, in particular, the segmentation problem (Paris & Durand, 2007; Gao *et al.*, 2013; Wu *et al.*, 2017). The topological summary comes naturally with a hierarchical structure that can be used in various clustering tasks, including the aforementioned image segmentation problem. Singh *et al.* (2007) also pointed out that this clustering feature will be useful in analyzing high-dimensional datasets. We believe that TDA has great potential in medical image segmentation.

In the TDA pipeline, a simplicial complex can be constructed as a topological space that approximates the underlying topology of the dataset. Nested complexes called *filtrations* can be introduced to describe the topology of the dataset at different scales. In a filtration, we control the scale by adjusting a scale parameter r . The *Morse-Smale complex* is a special complex constructed from the level sets of a density function f , whose scale parameter r is the threshold for the level sets. Details regarding this construction can be found in (Paris & Durand, 2007; Fasy *et al.*, 2014).

In Paris & Durand (2007), complexes based on super-level sets of estimated grayscale density function \hat{f} of images are constructed and TDA is performed. The scale parameter r is chosen to be related to the level, known as a boundary persistence parameter. The topological persistence for these types of complexes is used to separate the modes of the kernel density estimator \hat{f} constructed from an image. Intuitively, the more persistent a topological feature is in such a complex, the larger the difference between the interior and exterior grayscale density values of this level set (i.e., this particular feature is “well-defined”). Highly persistent features will indicate a sharper change of pixel density values, which more likely represents a boundary.

By increasing the threshold of the boundary persistence parameter defined by a difference of \hat{f} values between two different modes, we can construct a hierarchical clustering structure. Then, this persistence-based hierarchy describes the topological structure of the feature space. Clustering can be performed using this hierarchical structure, and then we select those modal regions which persist long enough in terms of the boundary persistence parameter. Regions whose boundary shows sharp contrast to its neighboring regions will be picked up by their method. We will choose this as our primary approach to extracting the topological information from the image, which is also the topology of the density estimator \hat{f} . We also point out that there exist other competing topological methods of segmentation based on certain types of representative cycles (Dey *et al.*, 2010; Gao *et al.*, 2013). These methods based are more closely related to the philosophy of treating contours as curves, instead of the clustering philosophy, but has the advantage of not assuming the additional mean-shift model (which will discussed further below).

In this paper, we perform extensive simulation studies and point out that when certain kinds of noise exists, this topological method based on the boundary persistence of the pixel density

estimator is not recommended. Also, we find that this method usually does not provide a smooth enough boundary, which is desired in certain applications.

1.3 Contours and Shape Analysis

As mentioned previously, image segmentation can also be formulated as a *contour detection*, or equivalently, curve estimation problem (Zhu & Yuille, 1996). In this setting, one treats the contour of a target object in the image as a curve in \mathbb{R}^2 , which minimizes some well-designed functional. We present a brief overview of active contours and statistical shape analysis, the latter of which is necessary to understand the models proposed by Joshi & Srivastava (2009); Bryner *et al.* (2013), for which we base our work on. We refer to Srivastava & Klassen (2016) for a comprehensive review for the theory and application of shape analysis.

Shape can be defined as the underlying structure of an object which is invariant to certain transformations deemed shape-preserving: rigid-motion and scaling. In other words, applying any combination of translation, rotation, and scale transformations may change the appearance of the object’s contour in \mathbb{R}^2 , but preserves its *shape*. Shape analysis research focuses on the representation of these objects in a way which respects these invariances, along with the development of statistical procedures for shape data. Early work in the field focused on the representation of shape by a set of finite, labeled points known as *landmarks*. These are typically selected by the researcher to represent locations on the object’s contour of mathematical and/or scientific significance. After landmark selection, statistical modeling proceeds using traditional multivariate techniques, with mathematical adjustments to account for the structure of the data. Kendall (1984) pioneered the landmark representation, with other key work by Bookstein (1986); Dryden & Mardia (1992); Small (1996); Dryden & Mardia (2016).

However, in the contour detection setting, it seems more natural to treat the underlying contour as a closed curve on \mathbb{R}^2 , parameterized by $\mathcal{D} = \mathbb{S}^1$, rather than as a set of finite labeled points. When extending the analysis to curves, the issue of registration becomes prominent. With landmarks, a correspondence of features across shapes is assumed by the order in which landmarks are specified. For curves, this correspondence is dictated by the curve’s parameterization. However, invariance of curves to parameterization is often desired, and is difficult to account for mathematically. Recent work in *elastic shape analysis* resolves these issues by exploiting parameterization invariance to allow for flexible re-parameterizations which optimally match points between curves, commonly referred to as *registration* (Kurtek *et al.*, 2012; Strait *et al.*, 2019). This allows for a more natural correspondence of features and improved statistical modeling of curves and shapes.

In the active contour approach, although the input is still the same (an image), the model treats the problem of segmentation as finding a 2-dimensional curve in the (larger) region $\Omega \subset \mathbb{R}^2$

that encompasses the clusters consisting of region C . A classical model from this perspective is proposed by Mumford & Shah (1989), in which the goal is to minimize the energy functional,

$$F(u, C) := \int_{\Omega} (u(x) - u_0(x))^2 dx + \mu \int_{\Omega \setminus C} |\nabla_x u(x)|^2 dx + \nu \text{vol } C, \quad (1.1)$$

over all piecewise smooth curves $u(x)$ in $\Omega \setminus C$, $C \subset \text{int } \Omega$, where $\text{vol } C$ is the volume of the area represented by C , and μ , ν are tuning parameters. The hope is that this finds the “correct” contour u which delineates the region C (Arbelaez *et al.*, 2011). The idea can be generalized as a Bayesian model which incorporates prior information (Joshi & Srivastava, 2009; Bryner *et al.*, 2013; Bryner & Srivastava, 2013), where the target energy functional to be minimized is now :

$$F(u, C) := \lambda_1 E_{\text{image}}(u) + \lambda_2 \int_{\Omega \setminus C} |\nabla_x u(x)|^2 dx + \lambda_3 E_{\text{prior}}(u). \quad (1.2)$$

This functional contains a term E_{image} which is only dependent on the image (i.e., the data). The term E_{prior} allows one to insert prior information about the knowledge of the shape of the region, which could have significant influence in the segmentation result (particularly if the region of interest is difficult to identify).

In this paper, we generate examples to show that when the object we want to target possesses a certain kind of topological structure, or there are multiple objects in the image, an active contour method will behave pathologically if not initialized appropriately. We illustrate that this issue is important with real data using the skin lesion data (Codella *et al.*, 2018). However, active contours can be robust to certain types of noise, whereas topologically-based methods may fail.

1.4 Topological and Contour Methods Revisited

As mentioned above, cluster and curve-based formulations of the segmentation problem result in very different perspectives in the current literature. We can directly estimate the regions which contain the segmented target, or we can estimate the closed curve contour which separates the segmented target from the background. One can represent the segmentation result by either the clustered set of pixels directly, or by the boundary pixels as “curves” that encapsulate the clusters.

In a topological data analysis approach, the topological information up to dimension 2 can be summarized by birth and death of the cycles in each dimension of approximating complexes. This approach treats the pixel values as being drawn from a grayscale density and then constructs the associated filtration induced by the level set of this density. This density-based approach is common to many classical segmentation methods (Huang & Dom, 1995; Zhu & Yuille, 1996; Monteiro & Campilho, 2006; Paris & Durand, 2007; Arbelaez *et al.*, 2011) and its performance

can be evaluated directly using the resulting clusters of points.

The TDA pipeline estimates clusters based on the filtration constructed from certain persistence parameters. In the model given in Paris & Durand (2007), topological information is extracted from the grayscale values f_i via a kernel density estimator. This information can help guide challenging segmentation tasks which may not work well under the classical energy model (Mumford & Shah, 1989). In order to evaluate the performance as a segmentation task, we can take the pixel points lying inside the obtained contour as the result of segmentation by the statistical shape model.

2 Model Specification and Implementation

In this section, we outline three different models for segmentation of an image. The first is a topologically-based method described by Paris & Durand (2007), which we abbreviate by TOP. The method of Bayesian active contours (BAC), as described by Joshi & Srivastava (2009); Bryner *et al.* (2013), is discussed after. The latter method treats segmentation as a curve estimation problem, with ideas from shape analysis used to allow for prior information to be incorporated. A performance comparison of these two methods under various image settings is discussed in Section 2.2, and is one contribution of this work. The final part of this section will outline our proposed method, TOP+BAC, which combines TOP with BAC in a very specific way to produce a “topologically-aware” segmentation.

2.1 Topological Segmentation (TOP)

In this section, we describe a topological segmentation method based on a mean-shift model assumption (Paris & Durand, 2007). First, we estimate the pixel density D by a kernel density estimator, using a Gaussian kernel G_σ . The bandwidth $\sigma = (\sigma_1, \sigma_2)$ of this Gaussian kernel G_σ is chosen separately on the subspace of the 2-dimensional pixel coordinates and the grayscale value g . *Topological persistence* is examined by constructing a filtration based on the estimated pixel density. In particular, given a level parameter τ , we form super-level sets $M_\tau := \{x \in \mathbb{R}^2 \mid D(x) \geq \tau\}$. This filtration yields a hierarchical clustering structure.

However, suppose that we know all the locations of maxima from the pixel density. Alternatively, one can compute the *boundary persistence* $p_b(m_1, m_2) := D(m_2) - D(s_{12})$ between two local maxima m_1, m_2 , satisfying $D(m_1) > D(m_2)$ with a saddle point s_{12} between these two points. Sets of pixels corresponding to boundary persistence greater than a pre-determined threshold T can be collected to form a hierarchical structure of clusters. Paris & Durand (2007) showed that the hierarchical structure provided by the boundary persistence is equivalent to the topological

persistence based on level sets of the density estimator. Thus, we can proceed by clustering based on boundary persistence, rather than calculating the whole filtration of super-level sets.

A natural question which arises with boundary persistence is how the locations of pixel density maxima are obtained. We can extract these pixel density modes by using the *mean-shift algorithm*, a classic method from cluster analysis. For a dataset $\mathcal{X} \subset \mathbb{R}^d$, the *sample mean* within the distance λ of $x \in \mathcal{X}$ is defined to be $m(x) := \frac{\sum_{y \in \mathcal{X}} \mathbf{1}_{\{\|x-y\| \leq \lambda\}} \cdot y}{\sum_{y \in \mathcal{X}} \mathbf{1}_{\{\|x-y\| \leq \lambda\}}}$, and the *mean-shift* at $x \in \mathcal{X}$ is defined to be $m(x) - x$ (Cheng, 1995). Intuitively, we first take the ‘‘average center’’ $m(x)$ of those observations that are lying within a λ -ball of the $x \in \mathcal{X}$, and then compute the deviation of x to this center. We can generalize these notions by replacing the flat kernel $K_x(y) = \mathbf{1}_{\{\|x-y\| \leq \lambda\}}$ with the Gaussian kernel, which we use exclusively in the rest of paper following Paris & Durand (2007). For the convenience of discussion, we define the *general sample mean* associated with kernel K as $m(x) := \frac{\sum_{y \in \mathcal{X}} K(x-y)w(y) \cdot y}{\sum_{y \in \mathcal{X}} K(x-y)w(y)}$, with weight function $w : \mathcal{X} \rightarrow (0, \infty)$.

Under this definition of the general sample mean, the mean-shift algorithm will iterate a point $x \in \mathcal{X}$ by the formula $x_{j+1} = \frac{\sum_{y \in \mathcal{X}} K(x_j-y)w(y) \cdot y}{\sum_{y \in \mathcal{X}} K(x_j-y)w(y)}$, generating a sequence of points $x_1 = x, x_2 = m(x), x_3 = m(m(x)), \dots$. It can be shown that the iterative algorithm stops when $m(\mathcal{X}) = \mathcal{X}$, i.e., the dataset has been mapped to its fixed points. The mean-shift sequence x_1, x_2, x_3, \dots corresponds to a steepest descent on the density $D(x) = \sum_{y \in \mathcal{X}} \tilde{K}(x-y)w(y)$, where \tilde{K} is the so-called *shadow kernel* associated with the kernel K (Cheng, 1995). As specified above, after performing the mean-shift algorithm to extract pixel density modes, we can then compute the boundary persistence, and obtain a hierarchical clustering structure by taking all modes with boundary persistence greater than T . We will indicate the parameters of TOP as (σ_1, σ_2, T) hereafter.

The resulting segmentation of TOP will be used as initialization of the gradient-descent algorithm in the active contour model, which is presented in Section 2.2. On one hand, we can regard TOP as an approach to initialize the active contour algorithm by providing useful topological information, stabilizing its result. On the other hand, we can regard the active contour method as a smoother of the TOP segmentation result.

2.2 Bayesian Active Contour (BAC)

2.2.1 Energy Functional Specification

We next describe segmentation by way of the Bayesian active contour (BAC) approach. Recall that active contours seek a contour curve u delineating the target object from the background by minimizing an energy functional. The model proposed by Joshi & Srivastava (2009); Bryner *et al.*

(2013); Bryner & Srivastava (2013) uses the following functional:

$$F(u) := \lambda_1 E_{\text{image}}(u) + \lambda_2 E_{\text{smooth}}(u) + \lambda_3 E_{\text{prior}}(u), \quad (2.1)$$

where $\lambda_1, \lambda_2, \lambda_3 > 0$ are user-specified weights. Contrary to the unsupervised TOP method of Section 2.1, the supervised BAC model assumes we have a set of *training images* with known ground truth object boundaries, and a set of *test images* on which we perform segmentation. The first two terms are fairly standard in the active contour literature.

The image energy term, E_{image} , is given by the following expression,

$$E_{\text{image}}(u) = - \int_{\text{int } u} \log(p_{\text{int}}(f(x, y))) dx dy - \int_{\text{ext } u} \log(p_{\text{ext}}(f(x, y))) dx dy,$$

where the $f(x, y)$ denotes the pixel density value at location (x, y) , and $\text{int } u$, $\text{ext } u$ denotes the interior and exterior regions of the curve, respectively. The quantities p_{int} , p_{ext} are kernel density estimates of pixel values for the interior and exterior of the true contour, respectively. In Joshi & Srivastava (2009); Bryner & Srivastava (2013); Bryner *et al.* (2013), these densities are estimated from training images, for which ground truth contours are known. From these, one can simply use a histogram (if the image is truly binary) or kernel density estimator (for general grayscale images) for pixel values that are found inside and outside the true contour, provided that the test image resembles training images in terms of pixel composition. Intuitively, we may interpret this image energy term as an entropy describing how sharp the contrast in the image is between the interior and exterior regions of a single curve u (Paragios & Deriche, 1999).

The smoothing energy term, E_{smooth} , for contour u is given by,

$$E_{\text{smooth}}(u) = \int_u |\nabla u(x, y)|^2 dx dy,$$

where $|\nabla u(x, y)|$ is the Jacobian of the curve at pixel coordinates (x, y) . This quantity is approximated numerically, given the discrete nature of an image. In general, the more wiggly u is, the larger E_{smooth} will be; thus, depending on the weight λ_2 prescribed to this term, one can control the desired smoothness of the solution.

The final term, E_{prior} , is the primary contribution of Joshi & Srivastava (2009); Bryner & Srivastava (2013); Bryner *et al.* (2013). This term quantifies the difference between the contour u and the mean shape of training curves, and choice of λ_3 controls how much u is pushed towards this training mean shape. This is useful in images where the object is not fully observable, for instance, in the presence of occluded boundaries or low signal-to-noise ratio. If one has training data available for a particular shape, then this term allows one to down-weight information provided by pixel values to push the contour towards the desired shape. To state the explicit form of this

term, we briefly discuss *elastic shape analysis*, methods which use a shape representation that is invariant to contour parameterization.

Parameterization-free representations of shape are necessary in the context of Bayesian active contours, as one must appropriately match features of the current contour to features of the training mean shape. Parameterization explicitly controls the correspondence of features across a collection of curves. Early work accounted for this by standardizing all curves to be arc-length parameterized (Zahn & Roskies, 1972; Younes, 1998; Klassen *et al.*, 2004). However, it has been noted that this imposes a strict, potentially unnatural correspondence of points between curves. Elastic shape analysis resolves this by finding an optimal correspondence between curves, allowing for a more natural registration of curves. We very succinctly outline details of this below and refer readers to articles by Joshi *et al.* (2007); Srivastava *et al.* (2011); Kurtek *et al.* (2012) and a book by Srivastava & Klassen (2016) for a more thorough discussion.

Suppose we have ground truth contours from training images denoted β_1, \dots, β_M , where $\beta_i : \mathcal{D} \rightarrow \mathbb{R}^2$. The goal of the prior energy term is to drive a contour u towards a “representative” shape based on β_1, \dots, β_M . To start with, we must first have an appropriate metric which is invariant to the various shape-preserving transformations (translation, rotation, scale, and re-parameterization, in the case of contours). In the elastic shape analysis literature, this is done by introducing the *square-root velocity function (SRVF)* $q : \mathcal{D} \rightarrow \mathbb{R}^2$ for a curve β , given by, $q(t) = \dot{\beta}(t)/\sqrt{|\dot{\beta}(t)|}$, where $|\cdot|$ is the Euclidean norm, $\dot{\beta}$ is the time-derivative of β , and $q(t) = 0$ wherever $\dot{\beta}(t)$ vanishes. This transformation is invertible, up to a translation of β , via $\beta(t) = \beta(0) + \int_0^t q(s)|q(s)| ds$.

In this setting, the shape of a curve β with SRVF q is given by the equivalence class: $[q] = \{O(q \circ \gamma)\sqrt{\dot{\gamma}} \mid O \in SO(2), \gamma \in \Gamma, q \in \mathcal{C}\}$ where $SO(2)$ is the special orthogonal group, Γ is the Lie group of re-parameterization functions $\Gamma = \{\gamma : \mathcal{D} \rightarrow \mathcal{D} \mid \gamma(0) = 0, \gamma(1) = 1, \dot{\gamma} > 0\}$, and \mathcal{C} is the space of all square-integrable curves q with unit norm. We proceed with some clarifications. First, given a rotation O and re-parameterization γ , we can apply these to the curve β to obtain the new curve $\tilde{\beta} = O(\beta \circ \gamma)$. The corresponding SRVF of $\tilde{\beta}$ is given by $O(q \circ \gamma)\sqrt{\dot{\gamma}}$ (i.e., members of the equivalence class $[q]$). This means that all SRVFs which only differ by a rotation and re-parameterization map to the same equivalence class $[q]$, which is desired as these transformations preserve shape. In addition, $[q]$ automatically accounts for the equivalence of the shapes of curves only differing by a translation and scale, since SRVFs are translation-invariant (due to their dependence on $\dot{\beta}$), and we restrict the space of SRVFs to be of unit norm (i.e., \mathcal{C}). This last statement allows one to analyze SRVFs on the infinite dimensional Hilbert sphere, for which we have an explicit distance formula. Finally, the space of all equivalence classes is known as the *shape space* \mathcal{S} , formally defined as the quotient structure $\mathcal{C}/(SO(2) \times \Gamma)$. The *elastic shape*

distance between $[q_1], [q_2] \in \mathcal{S}$ is defined as:

$$d_{\mathcal{S}}([q_1], [q_2]) = \cos^{-1} \left(\langle \langle q_1, q_2^* \rangle \rangle \right) \quad (2.2)$$

where $q_2^* = O^*(q_2 \circ \gamma^*) \sqrt{\gamma^*}$ and $(O^*, \gamma^*) = \underset{O \in SO(2), \gamma \in \Gamma}{\operatorname{argmin}} \cos^{-1} \left(\langle \langle q_1, O(q_2 \circ \gamma) \sqrt{\gamma} \rangle \rangle \right)$, for $q_1, q_2 \in \mathcal{C}$. The latter optimization problem is known as the *registration problem*, and solving it amounts to finding the rotation and re-parameterization of q_2 which optimally matches the fixed q_1 . The optimal rotation O^* has an explicit solution, while γ^* is approximated using a dynamic programming algorithm. Implementation details are discussed in Srivastava *et al.* (2011). This distance is related to the *elastic metric*, which measures the amount of infinitesimal bending and stretching when deforming one shape to another.

We now introduce a notion of the “mean shape” to be used for the E_{prior} term in the BAC model, we assume that the training curves are observed in the form of N points in \mathbb{R}^2 , stored as a $2N$ -dimensional vector. The quantity N is the discretization size of the contour. Typically, $N = 100$ or $N = 200$ is sufficient to capture small shape features. The *sample Karcher mean* of training shapes $[q_1], \dots, [q_M]$ is defined by the SRVF of a curve \bar{q} such that $[\bar{q}] = \arg \min_{[q] \in \mathcal{S}} \sum_{i=1}^M d_{\mathcal{S}}([q], [q_i])^2$. This is analogous to the usual sample mean, which uniquely minimizes the sum of squared deviations in Euclidean space. Unfortunately, the shape space \mathcal{S} is nonlinear and possesses a quotient structure, and thus, no explicit solution exists for this optimization problem; in fact, uniqueness is not even guaranteed. However, one can numerically find a local minimum via a gradient-descent algorithm, as described by Srivastava *et al.* (2011); Kurtek *et al.* (2012). Once the sample Karcher mean shape $[\bar{q}]$ is computed, we can examine shape variation by computing the second moments. Since tangent spaces are linear, covariance matrices can be computed in the traditional sense by projecting observations to the tangent space centered at $[\bar{q}]$, denoted $T_{[\bar{q}]}(\mathcal{S})$. Let $v_1, \dots, v_M \in T_{[\bar{q}]}(\mathcal{S})$, where $[\bar{q}]$ is the training sample Karcher mean, and $v_i = \exp_{[\bar{q}]}^{-1}([q_i])$ for $i = 1, \dots, n$ be tangent vectors representing the n sample shapes (for which an explicit formula, known as the inverse-exponential map, is known). The *sample Karcher covariance* is defined as $\hat{K} = \frac{1}{M-1} \sum_{i=1}^M w_i w_i^\top$, where $w_i = \operatorname{vec}(v_i)$ converts the $2N$ -dimensional vector to a $2N$ -dimensional column vector by concatenating the two rows. Dominant modes of shape variation are found by performing singular value decomposition of the sample Karcher covariance of training images (i.e., expressing $\hat{K} = U \Sigma U^\top$, where U is the matrix of eigenvectors corresponding to the diagonal matrix Σ of eigenvalues).

This decomposition allows one to incorporate prior object segmentation information via a formal probability model. To do this, select the first m columns of U which correspond to the largest m eigenvalues. We call these truncated matrices U_m and Σ_m , respectively. Then, the prior

energy term is given by:

$$E_{\text{prior}}(u) = \frac{1}{2}w^T(U_m\Sigma_m^{-1}U_m^\top)w + \frac{1}{2\delta^2}|w - U_mU_m^\top w|,$$

where $w = \exp_{[\bar{q}]}^{-1}([q])$ is the tangent vector in $T_{[\bar{q}]}(\mathcal{S})$ corresponding to contour u (with SRVF q), U_m, Σ_m are the leading m eigen-component pairs in the singular value decomposition of the empirical Karcher covariance matrix \hat{K} for the training shapes, and δ is selected to be less than the smallest eigenvalue in Σ_m . This prior energy term is equivalent to the log-likelihood of a truncated wrapped Gaussian density on \mathcal{S} . If the contour u is not very close to the training mean shape $[\bar{q}]$, then $E_{\text{prior}}(u)$ will be large.

2.2.2 Gradient-Descent

The standard way to minimize the energy functional in Equation 2.1 is via a gradient-descent algorithm. Given current contour $u^{(i)}$, we update by moving along the negative gradient of F as follows:

$$u^{(i+1)}(t) = u^{(i)}(t) - \lambda_1 \nabla E_{\text{image}}(u^{(i)}(t)) - \lambda_2 \nabla E_{\text{smooth}}(u^{(i)}(t)) - \lambda_3 \nabla E_{\text{prior}}(u^{(i)}(t)).$$

Updates proceed sequentially until the energy term stabilizes (i.e., the rate of change of the total energy is below some pre-specified convergence tolerance), or a maximum number of iterations is reached. This requires specification of an initial contour $u^{(0)}$, which can be chosen in many different ways. Unfortunately, as gradient-descent only is guaranteed to find local extrema, final segmentations can be extremely sensitive to the choice of initialization curve $u^{(0)}$.

The first two gradient terms are given by:

$$\begin{aligned} \nabla E_{\text{image}}(u^{(i)}(t)) &= -\log\left(\frac{p_{\text{int}}(f(u^{(i)}(t)))}{p_{\text{ext}}(f(u^{(i)}(t)))}\right)n(t) \\ \nabla E_{\text{smooth}}(u^{(i)}(t)) &= \kappa_{u^{(i)}}(t)n(t), \end{aligned}$$

where $n(t)$ is the outward unit normal vector to $u^{(i)}(t)$, and $\kappa_{u^{(i)}}$ is the curvature function for $u^{(i)}$. At a particular point along the contour $u^{(i)}(t)$, the image update moves this point inward along the normal direction if $p_{\text{int}}(f(u^{(i)}(t))) < p_{\text{ext}}(f(u^{(i)}(t)))$, meaning that this current image location is more likely to be outside the contour than inside (with respect to the estimated pixel densities p_{in} and p_{out}). If the opposite is true, then the point on the contour is updated outward along the normal direction, ‘‘expanding’’ the contour. The smoothness update uses curvature information to locally smooth the curve. Without the action of other energy updates, this term will push any

contour towards a circle.

The shape prior update term is more complicated. In order to obtain $\nabla E_{\text{prior}}(u^{(i)}(t))$, first compute the gradient vector $a = (U_m \Sigma_m^{-1} U_m^\top + (I - U_m U_m^\top) / \delta^2) w$, where $w = \exp_{[\bar{q}]}([q^{(i)}])$ for SRVF $q^{(i)}$ corresponding to $u^{(i)}$, and again, δ is chosen to be less than the smallest eigenvalue in Σ_m . This update is computed on $T_{[\bar{q}]}(\mathcal{S})$; however, we wish to update the curve $u^{(i)}$ (instead of $[\bar{q}]$), and thus, must parallel transport this gradient vector to $T_{[q^{(i)}]}(\mathcal{S})$. Similar to Bryner *et al.* (2013), call this new vector $b = \Pi(a : [\bar{q}] \rightarrow [q^{(i)}])$, where Π denotes the parallel transport operator (an expression of which is known for spherical spaces). This yields an updated vector to apply to the SRVF $q^{(i)}$, but ultimately, one wants to apply this update to the *curve* $u^{(i)}$. This is done as follows:

1. Move a small amount along the negative gradient direction $-b$ via the exponential map: $q_{\text{new}} = \exp_{[q^{(i)}]}(-\epsilon b)$, for ϵ small.
2. Map back to its curve representation β_{new} .
3. Re-scale and translate β_{new} to have the same length and centroid as $u^{(i)}$.
4. Define prior update $\nabla E_{\text{prior}}(u^{(i)})(t) = \frac{1}{\epsilon}(u^{(i)}(t) - \beta_{\text{new}}(t))$.

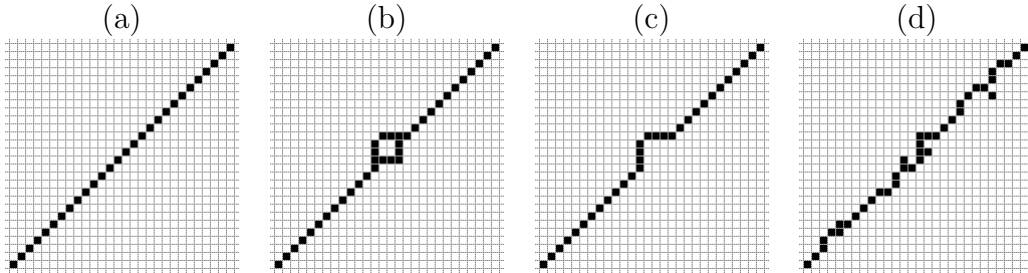
This conversion back to the original curve representation is necessary so that the update can be combined with the image and smoothness update terms, which are defined based on the original contour (rather than SRVFs). Hereafter, we will indicate the parameters of BAC as $(\lambda_1, \lambda_2, \lambda_3)$.

2.3 Bayesian Active Contour with Topological Initialization (TOP+BAC)

As noted in Section 2.2, Bayesian active contours require a gradient-descent algorithm with initially-specified contour $u^{(0)}$. As noted earlier, since gradient-descent searches for local extrema, there is no guarantee that the final contour represents the target of interest. In addition, many images feature objects with more complex topological structure (e.g., objects with multiple connected components and/or holes within). We propose a new approach, Bayesian active contours with topological initialization (TOP+BAC), as a combination of the methods from Sections 2.1 and 2.2. This addresses both issues:

1. TOP can provide an automatic way of initializing a single contour, in the hope that initialization sensitive gradient-descent converges efficiently to correct target.
2. TOP can be used to initialize multiple active contours simultaneously, for object boundaries which cannot be represented by a single curve due to its topological nature.

Figure 2.1: Different image of the same diagonal straight lines, with different sources of noises.



TOP+BAC can be thought of as using TOP to provide a loose segmentation which is able to identify topological features of interest, followed by enhancing those results by using BAC in order to provide a finer segmentation. This allows one to increase the interpretability and consistency in terms of topological invariants.

Before we are over-optimistic about the proposed method that combines TOP and BAC, we illustrate the drawbacks of each of TOP and BAC individually by considering simple images in Figure 2.1. Case (a) is exactly a straight line, while case (b)-(d) are straight lines with various kinds of noises. The BAC model will roughly identify all these pixel images as one straight line contour with a certain degree of smoothness. However, TOP will identify (a) and (c) as a straight line contour, but (b) as a contour with a cycle in the middle of it. In the case of a noisy image like (d), TOP will be highly sensitive to the “noise points”. This will be witnessed by an unstable segmentation result for a small perturbation in parameters of the TOP method (see also Figure 4.2). However, with a reasonable initialization, the BAC result usually gives a rather accurate segmentation result. On the other hand, BAC is incapable of segmenting images with multiple objects or with only one topologically non-trivial object. Thus, we hope to exploit the strengths of both of these methods by proposing TOP+BAC.

Currently, it appears that there is not an agreed generalization of active contour methods into multiple object images with non-trivial topological structures (e.g., an image with numerous donuts). Using the proposed two-step method, we can extend most current active contour type methods into multiple object images, as the TOP method provides a natural partition of the images into several regions, where only one object lies in each region. We can also segment a single topologically complex object by performing separate active contour algorithms on components identified by the topological method. In addition, by treating each topological feature as a separate curve, one can then incorporate prior information in BAC and control smoothness separately for each curve, which cannot be achieved by using TOP alone.

We note that TOP+BAC does lead to increased computational cost, which may not be desirable for all segmentation tasks. However, if an interpretable segmentation which respects the underlying

topological structure is of utmost importance, TOP+BAC will improve on results via TOP or BAC individually. Also, when prior information is not close to ground truth, BAC can converge very slowly, or even not converge at all, to the ground truth for certain choices of λ_3 (see the plot of performance measure vs. converging steps, in Supplementary Materials). If we take the segmentation result of TOP and use it as an initialization on multiple regions of the image, then with a reasonable shape prior, BAC will capture all of the contours with such a prior information regardless of noise.

3 Performance Evaluation Measures for the Segmentation Problem

To evaluate the performance of the segmentation result, we need to choose appropriate performance evaluation measures that compare our segmentation with the *ground truth* of the image (Abdulrahman *et al.*, 2017), which is the true segmentation. As we mentioned, the output of the contour comes in two different forms, depending on the methods: TOP yields clusters of pixel points, whereas BAC and TOP+BAC will produce contours representing the boundaries of the segmented regions. If we simply want to compare the contours of the segmentation clusters, then an appropriate measure should be defined on the space of all possible curves (with potentially multiple connected components).

A comprehensive introduction of several performance evaluation measures has been given by Zhang (1996). All performance measures for image segmentation were categorized as analytical, empirical goodness or empirical discrepancy measures. *Analytical measures* evaluate the performance by the model used for image segmentation task. In our case, geometric and topological information is difficult to characterize, and therefore it is difficult to come up with an analytic measure. Empirical goodness or empirical discrepancy methods are tied to the output of the segmentation, regardless of the model assumption. *Empirical goodness measures* focus on goodness metrics such as uniformity within or between segmented regions. These measures examine the output segmentation itself and do not require comparison to the ground truth of an image. On the other hand, *empirical discrepancy measures* characterize the difference between segmentation and ground truth quantitatively. In a more recent work, Monteiro & Campilho (2006) reviewed these empirical goodness and discrepancy types of measures and classify them as region-based and boundary-based measures. Most performance evaluation measures (Zhang, 1996; Monteiro & Campilho, 2006; Abdulrahman *et al.*, 2017) assume the segmentation result and truth come in form of clusters. In this case, the objects under comparison are two collections of regions consisting of pixel points. In simulation studies, we convert the contour curves into pixel clusters in

images by taking its interior. We will focus on empirical discrepancy measures which compare the segmentation results with ground truth. We give a very brief introduction of each measure we consider below.

3.1 Hausdorff Distance

The Hausdorff distance can be used to measure how close two sets are in a metric space. Let A and B be two non-empty subsets of a metric space (M, d) . We define their Hausdorff distance $d_H(A, B)$ by,

$$d_H(A, B) = \max\left\{\sup_{x \in A} \inf_{y \in B} d(x, y), \sup_{y \in B} \inf_{x \in A} d(x, y)\right\},$$

where $d(\cdot, \cdot)$ is the metric distance. Equivalently, the Hausdorff distance can be written as $d_H(A, B) = \inf\{\epsilon \geq 0; A \subseteq B_\epsilon \text{ and } B \subseteq A_\epsilon\}$, where $A_\epsilon := \bigcup_{x \in A} \{z \in M; d(z, x) \leq \epsilon\}$. We use this as a naive measure between the point sets of segmentation result and the ground truth. Hausdorff distance reflects both local and global discrepancy between two point sets, so we expect it to be an overall measure of discrepancy between two sets of points in the same space \mathbb{R}^2 . The set A refers to the clusters of the estimated region and set B consists of the points from the ground truth clustering.

3.2 Hamming Distance

Huang & Dom (1995) introduced the idea of the (directional) Hamming distance between two segmentations consisting of clusters. Let the directional distance between two segmentations $S_1 = \{s_1^1, \dots, s_1^n\}$, $S_2 = \{s_2^1, \dots, s_2^m\}$ be given by:

$$D_H(S_1 \rightarrow S_2) := \sum_{\{i; s_2^i \in S_2\}} \sum_{\{(k, j); s_1^k \neq s_1^j, s_1^k \cap s_2^j \neq \emptyset\}} |s_2^i \cap s_1^k|.$$

A region-based performance evaluation measure based on normalized Hamming distance is defined as,

$$p_H(S_1, S_2) := 1 - \frac{D_H(S_1 \rightarrow S_2) + D_H(S_2 \rightarrow S_1)}{2 \cdot |S|},$$

where $|S|$ is the image size. Here, we take S_1 as the estimated region A and S_2 as the ground truth region B .

3.3 Jaccard Distance

The Jaccard index metric (Jaccard, 1901; Späth, 1981), also known as the Jaccard similarity coefficient, is a widely used measure (Arbelaez *et al.* (2011)). The Jaccard coefficient measures similarity between finite sample sets; in our case, the clusters from the final segmentation, and is given by:

$$J(A, B) = \frac{|A \cap B|}{|A \cup B|} = \frac{|A \cap B|}{|A| + |B| - |A \cap B|},$$

where we regard A as the estimated region and B as the ground truth. If A and B are both empty, we define $J(A, B) = 1$. One can use the Jaccard distance to measure dissimilarity between sample sets, by defining $d_J(A, B) = 1 - J(A, B)$. This latter distance is what we will use throughout this paper.

3.4 Discovery Rates

Since we regard the problem of interest as a curve or region estimation problem over an image, a natural measure of such an approach is the false positive rate, treating each pixel as an estimation location. In this direction, Abdulrahman *et al.* (2017) suggests the performance measure,

$$PM(A, B) = 1 - \frac{TP}{TP + FP + FN},$$

where if we regard A as the estimated region and B as the ground truth, the quantities shown in the formula above can be summarized as follows: $TP = |A \cap B|$ (true positive); $FP = |A \cap B^c|$ (false positive); $FN = |A^c \cap B|$ (false negative).

3.5 Elastic Shape Distance

Finally, since the result of the proposed TOP+BAC algorithm is an estimated contour, we can compare this to the true contour's shape by computing their elastic shape distance, which was defined in Section 2.2.1. Given true contour β_{true} and estimated contour β_{est} with SRVFs q_{true} and q_{est} , respectively, then recall that the elastic shape distance is given by:

$$d_S([q_{\text{true}}], [q_{\text{est}}]) = \underset{O \in SO(2), \gamma \in \Gamma}{\operatorname{argmin}} \cos^{-1} \left(\langle \langle q_{\text{true}}, O(q_{\text{est}} \circ \gamma) \sqrt{\dot{\gamma}} \rangle \rangle \right),$$

where $\langle \langle \cdot, \cdot \rangle \rangle$ is the \mathbb{L}^2 inner product. Note that this does not take pixel position into consideration, and so if the estimated contour is simply translated to a different portion of the image, the elastic

shape distance will not change. However, this quantifies shape dissimilarity within the image, which can be useful in certain applications. Also note that for topologically non-trivial objects with boundaries represented by multiple contours, we can simply compute the elastic shape distance between corresponding estimated and ground truth contours separately.

4 Data Analysis

In this section, we apply the proposed method to several simulated images, as well as real data. We begin by looking at a binary image of an object with a single connected component and no loops, the most simple topological structure. We demonstrate that BAC, TOP, and TOP+BAC all identify the true boundary contour very well in this situation, as expected. In practice, images are usually contaminated with some noise. Thus, we follow with an investigation into how these methods perform when the original binary image is polluted with several types of noise. Then, we extend the simulation to an object with more complex topological structure, and show that TOP+BAC is necessary to identify the multiple boundaries which are present in such an object. We conclude with a study of skin lesion data Codella *et al.* (2018), which feature images with multiple connected components.

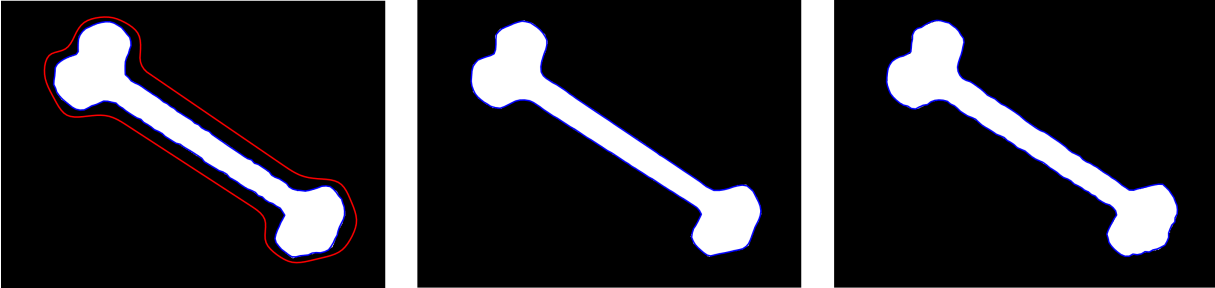
4.1 Simulation Studies for Object with Trivial Topological Features

4.1.1 Binary Image with No Noise

To begin, consider bone images selected from MPEG-7 dataset, referenced in Bai *et al.* (2009), among others. In this setup, we start with the contours of 20 bone curves (represented by $N = 200$ points each), and construct binary images with the interior of each bone in white, and the exterior in black. To examine the performance of contour detection under the model discussed in Section 2, we select one image as the test image, leaving the remaining 19 as training images. Since the images have been constructed based on the underlying bone contours, we have ground truth segmentations for both training and test sets, thus allowing us to quantify performance of the aforementioned algorithms by comparing the ground truth to estimated segmentations using different performance measures. For binary images, we can estimate the interior and pixel densities using a histogram estimator.

Figure 4.1 shows the final segmentation under the BAC, TOP and TOP+BAC approaches. For BAC, we selected $\lambda_1 = 0.3$, $\lambda_2 = 0.3$, and $\lambda_3 = 0$ (i.e., no shape prior update). For TOP, we selected $\sigma_1 = 5$, $\sigma_2 = 5$, $T = 5$ (i.e., select all topological features with boundary persistence greater than 5). We argue that a shape prior is not necessary for a simple binary image, since it is

Figure 4.1: Final segmented contour (in blue) for a binary, no-noise bone image using BAC (left), TOP (middle), and TOP+BAC (right). The left panel also shows the BAC initialization in red. BAC methods are performed using $\lambda_1 = 0.3$, $\lambda_2 = 0.3$, $\lambda_3 = 0$; TOP methods are performed using $\sigma_1 = 5$, $\sigma_2 = 5$, $T = 5$. Using a convergence tolerance of 10^{-7} , BAC requires 27 steps to converge, while TOP+BAC requires 7 steps.



clear what the target object is to be segmented. The choice of the update parameters is pedagogic, in the presence of no shape information a priori and a clearly identified object, we suggest setting $\lambda_3 = 0$, allowing the image and smoothness terms to guide the updates of the active contour. The image update parameter λ_1 can be chosen somewhat subjectively, especially for a simple binary image. One should select λ_1 large enough that the algorithm does not update too slowly; however, choosing λ_1 to be large can potentially result in the introduction of self-intersections of the contour (See Fig. ?? in Supplementary Materials), particularly in regions of high curvature. We have found that selecting λ_1 between 0.15 and 0.5 is generally appropriate for many of the images we have examined. The smoothing parameter λ_2 is chosen relatively small here, as the boundary is already fairly smooth here. This can, however, be adjusted by the user to ensure a final contour which does not have many small bumps.

As stated earlier, the BAC algorithm requires an initialization of the contour, and can be highly sensitive to this specification. Thus, for BAC, we hand-selected the contour which is shown in red on the leftmost panel of the Figure 4.1. However, TOP+BAC uses the TOP result to initialize the contour. In this case, the method works well, as the result of the mean-shift algorithm is a contour which is essentially right where the true boundary occurs (as shown in the middle and right panel of Figure 4.1), and TOP correctly identifies the objects’s topological structure. In this setting, TOP may be the best tool of use, as BAC methods rely on gradient updates, which can introduce slight numerical errors to the estimated contour. TOP+BAC is not necessary, as the image features a topologically-trivial object, and TOP by itself segments this object well. The left panel of Table 1 shows performance metrics from Section 3 evaluated for the segmentation results using BAC, TOP, and TOP+BAC. Note that for all measures, the results are quite comparable, which is confirmed visually. Further results under various choices of λ_1 , λ_2 , λ_3 are found in the Supplementary Materials.

Table 1: Performance metrics for the BAC, TOP, and TOP+BAC (abbreviated TAC in the table) methods applied to the (1) binary, no-noise bone image from Figure 4.1, (2) the bone image with Gaussian contour perturbations from Figure 4.3, and (3) the Gaussian blur bone image from Figure 4.6. From top to bottom, measures are Hausdorff distance, Hamming distance, Jaccard distance, performance measure based on discovery rates, and the elastic shape distance. In bold, the optimal method for each measure is displayed.

Measure	(1)			(2)			(3)		
	BAC	TOP	TAC	BAC	TOP	TAC	BAC	TOP	TAC
d_H	4.6904	4	3.7417	4.6904	4.1231	3.7417	4.5826	5.6569	4.8990
p_H	0.0031	0.0046	0.0031	0.0030	0.0049	0.0033	0.0040	0.0043	0.0066
d_J	0.0204	0.0312	0.0208	0.0216	0.0346	0.0228	0.0291	0.0316	0.0445
PM	0.0251	0.0369	0.0246	0.0249	0.0406	0.0270	0.0316	0.0335	0.0507
d_S	0.0985	0.0606	0.0909	0.1162	0.0637	0.0909	0.0711	0.1251	0.0712

4.1.2 Binary Image with Binary Noise

Next, we add two different types of binary noise to the binary bone image. First, consider adding (binary) salt-and-pepper noise (Marques, 2011). This is done in MATLAB using the `imnoise` function (with a pre-specified noise density, for which we select its parameter to be 0.3), perturbing the image by adding black pixels to the interior, and white pixels to the exterior. Since the resulting image is still binary, we can still perform image updates by estimating interior and exterior pixel densities using the histogram estimator.

In Figure 4.2, we illustrate some issues that arise for segmentation of this image under BAC and TOP methods. The left panel shows a BAC run from a pre-specified initial contour, with the same parameter settings as the image with no noise. Due to the artificial noise, contour updates are much slower and lead to less smooth updates throughout the course of the algorithm. After 300 iterations, we see a final contour which has captured most of the bone’s boundary, but still requires additional iterations to fully converge. This can be solved by drawing an initial contour which is even closer to the truth, or allowing the algorithm to run longer. Unfortunately, we cannot use an automatic topological initialization via TOP, due to the resulting boundary image shown in the right panel of Figure 4.2. The algorithm finds many small boundaries due to the noise in the image; we generally hope to initialize TOP+BAC by the largest connected component (in terms of size) from this map in TOP, but this is not feasible. Thus, we recommend using BAC over TOP in this setting. One should note that the amount of this type of noise is quite rare in real image applications, particularly in the background of a scene.

Instead of perturbing image pixel values, we can also perturb the underlying contour by simply adding a bivariate Gaussian random number to each column (corresponding to Euclidean coordi-

Figure 4.2: Left: Final segmented contour (in blue) for a salt-and-pepper noisy bone image using BAC, with initialization in red. BAC methods are performed using $\lambda_1 = 0.3$, $\lambda_2 = 0.3$, $\lambda_3 = 0$; TOP methods are performed using $\sigma_1 = 5$, $\sigma_2 = 5$, $T = 5$, and the final contour after 300 iterations (the pre-specified maximum) is shown. Right: Resulting boundary map under TOP. Note that, due to the large amount of noise, it is impossible to identify a single connected component for which we can use to initialize TOP+BAC.

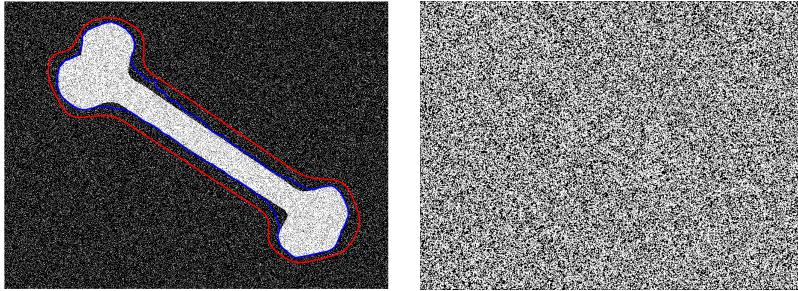
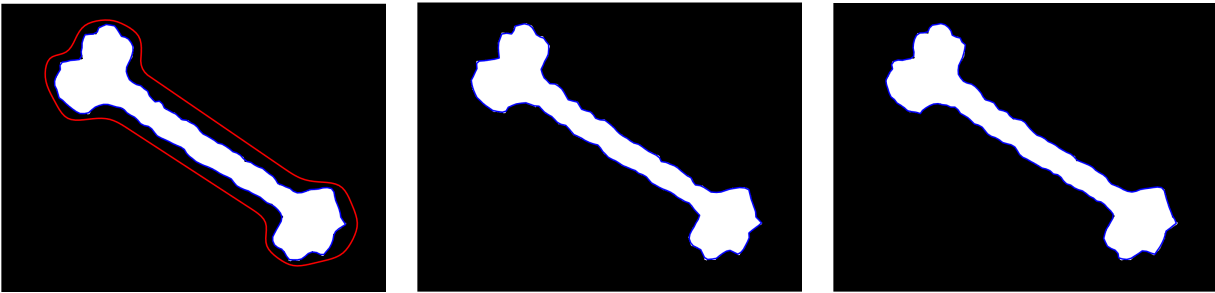


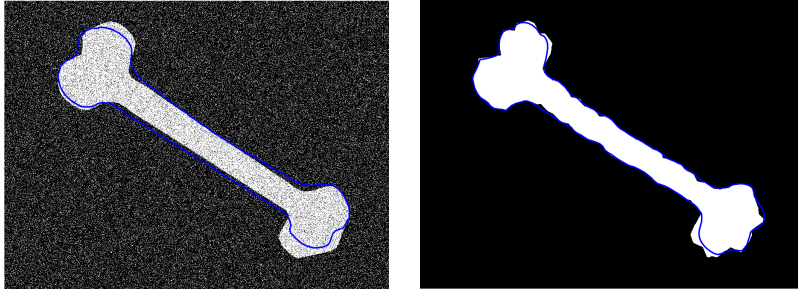
Figure 4.3: Final segmented contour (in blue) for a binary, no-noise, perturbed bone image using BAC (left), TOP (middle), and TOP+BAC (right). The left panel also shows the BAC initialization in red. BAC methods are performed using $\lambda_1 = 0.3$, $\lambda_2 = 0.3$, $\lambda_3 = 0$; TOP methods are performed using $\sigma_1 = 5$, $\sigma_2 = 5$, $T = 5$. Using a convergence tolerance of 10^{-7} , BAC requires 31 steps to converge, while TOP+BAC requires 7 iterations.



nates) of the vector representing the underlying \cdot . This creates a jagged bone from the smooth bone contour (See Figure 4.1.2). However, since the image is still binary and has no noise, we expect BAC, TOP, and TOP+BAC to perform equally well; this is the case, as illustrated in Figure 4.3, with identical BAC settings $\lambda_1 = 0.3$, $\lambda_2 = 0.3$, $\lambda_3 = 0$ and TOP setting $\sigma_1 = 5$, $\sigma_2 = 5$, $T = 5$. Corresponding performance measures are found in the middle portion of Table 1.

The effect of the prior term on gradient updates in active contour algorithms is crucial for both of these examples. In the image with salt-and-pepper noise, judicious use of prior shape knowledge can help drive the update towards a suitable contour in many fewer iterations than without a shape prior. This is because the prior term only involves the contour information from ground truth segmentations of training images, without any regard for the signal-to-noise ratio within the image itself. This is shown in the left panel of Figure 4.4, where we now set $\lambda_3 = 0.05$.

Figure 4.4: Final segmented contour (in blue) using BAC for (left) salt-and-pepper-noised bone image and (right) perturbed bone image, with settings $\lambda_1 = 0.3$, $\lambda_2 = 0.3$, $\lambda_3 = 0.05$. Using a convergence tolerance of 10^{-7} , the algorithm converged in 34 and 20 steps, respectively.



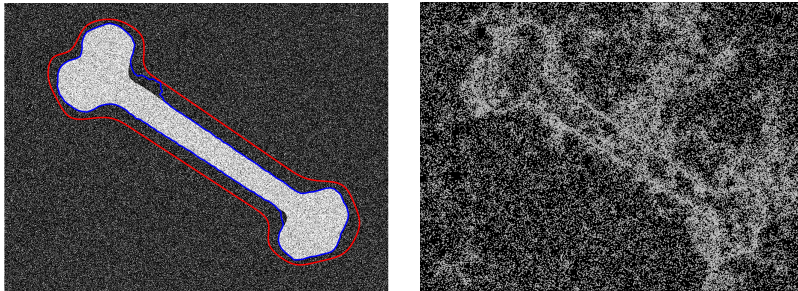
Note that within 34 steps, the BAC algorithm has converged. While the targeted bone does not perfectly match the shape in the image, we obtain a biased estimate which ignores the noise to some degree. On the right panel, we illustrate the idea that use of the prior can also help average out the random noise along the boundary when segmenting the test image, producing a smooth final contour despite results from TOP or traditional active contour methods a jagged contour. A decision of whether to use the prior term is application-specific; for most images, we suggest setting $\lambda_3 = 0$, particularly when a topological initialization is used. However, if the full object is not correctly observable in the image, whether due to binary noise along the boundary or occluded features as remarked by Bryner *et al.* (2013), use of a prior term can be beneficial to segmentation.

4.1.3 Binary Image with Non-Binary Noise

Next, we look at adding non-binary noise to the original binary bone image, as this is a more common source of noise for images arising from standard applications. This means that these new grayscale images will take pixel values between 0 and 1, rather than *only* 0 or 1. To accommodate this, we now use kernel density estimates rather than histogram estimates, of interior and exterior pixel intensities in order to perform updates using the image energy term. We consider two different types of non-binary noise pollution to the image: Gaussian noise (using the MATLAB function `imnoise`) and Gaussian blur (MATLAB function `imgaussfilt`).

We use the same setting for TOP methods in this simulation, but a different choice of BAC parameters. The left side of Figure 4.5 shows the result of BAC on the bone image perturbed by Gaussian pixel noise. Just like in Figure 4.2, updates of the active contour do eventually lead to most of the bone being segmented correctly, but the algorithm requires many steps to move around the noisy background. Note that in this case, the algorithm has converged under our stopping criterion (which can be set even smaller if a better contour is desired). However, this cannot be

Figure 4.5: Left: Final segmented contour (in blue) for a Gaussian noise-added bone image using BAC, with initialization in red. BAC settings are $\lambda_1 = 0.3$, $\lambda_2 = 0.3$, $\lambda_3 = 0$, while TOP settings are $\sigma_1 = 5, \sigma_2 = 5, T = 5$. Using a convergence tolerance of 10^{-7} , BAC converges after 143 iterations. Right: Resulting boundary map under TOP. Note that, due to the large amount of noise, it is impossible to identify a single connected component for which we can use to initialize TOP+BAC.



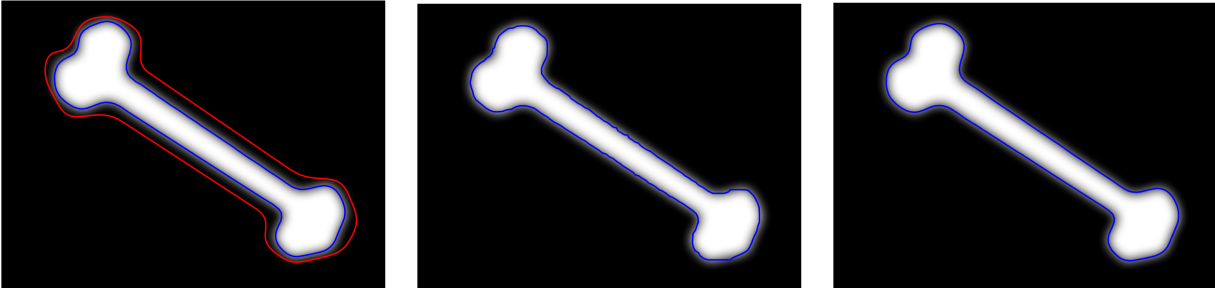
improved by a topological initialization, as the boundary map produced via TOP is also difficult to utilize, and in particular, a single connected component for which to initialize TOP+BAC is not easily identifiable. Thus, with a large amount of non-binary noise, we do not recommend use of TOP or TOP+BAC in this non-binary setting. Similar to the salt-and-pepper noisy image, one can set $\lambda_3 > 0$ in BAC to help the contour update with less emphasis on the added pixel noise, if some bias in the estimate is deemed acceptable.

Finally, we also consider applying Gaussian blur to the binary bone image, which makes boundary identification more challenging. The blurring effect at the boundary requires us to be less aggressive with image updates (i.e., downweight λ_1), due to the behavior of the estimated interior and exterior pixel densities. Note that BAC and TOP perform well on their own, and that TOP+BAC helps to smooth out some of the small bumps that are visible in the TOP segmentation. Since the result of TOP is dependent on the specified parameters, this can lead to results which either capture the bone perfectly, or perhaps capture a bone shape which is slightly larger than the truth. In this case, using this as an initialization for TOP+BAC allows one to refine the segmentation towards the true contour by using the estimated pixel densities from training images. The right panel of Table 1 shows performance measures for this example.

4.2 Simulation Studies for Objects with Non-Trivial Topological Features

In the previous simulations, we have looked at a binary bone image which has been contaminated with various types of noise. In some settings, TOP is hopeless while BAC renders itself somewhat useful, while in other cases, TOP performs as well or slightly better than BAC. However, in all

Figure 4.6: Final segmented contour (in blue) for a bone image with artificial Gaussian blur using BAC (left), TOP (middle), and TOP+BAC (right). The left panel also shows the BAC initialization in red. BAC methods are performed using $\lambda_1 = 0.3$, $\lambda_2 = 0.3$, $\lambda_3 = 0$; TOP methods are performed using $\sigma_1 = 5$, $\sigma_2 = 5$, $T = 5$. Using a convergence tolerance of 10^{-7} , BAC converges in 59 steps, while TOP+BAC requires 37 iterations.



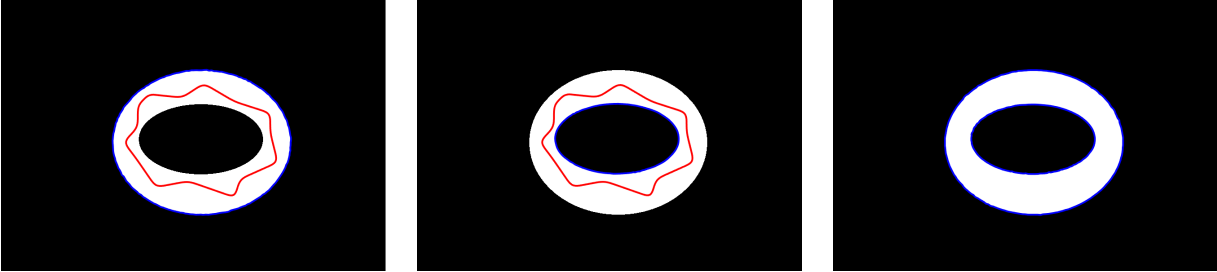
of these cases, a topological initialization for active contour algorithms does not seem to result in much improvement. This is because the underlying object in the image is trivial in a topological sense (i.e., one connected component with no hole). To explore the true potential of the TOP+BAC method, we now consider artificially-constructed donut images, which have a more complex topological structure due to the presence of two boundaries and one hole in the middle.

4.2.1 Binary Image with No Noise

First we consider a binary donut image as test image, which has been artificially constructed from two curves, so that the ground truth boundaries are known beforehand. In order to estimate pixel densities, we also form 9 more binary donut images as training images, formed from sets of ground truth curves. Each donut consists of a large, outer boundary, and a smaller, inner boundary, and we assume that the labels of ground truth curves (i.e., outer or inner boundary) from the training images are known. If this is the case, we estimate the interior and exterior pixel densities $p_{\text{int}}^{(j)}$ and $p_{\text{ext}}^{(j)}$ for $j = 1$ (outer contour curve) and $j = 2$ (inner contour curve) marginally.

We first demonstrate the inability for BAC to correctly account for the topological structure of this donut image. To do so, we initialize a single curve within the white region of the donut image, and apply the usual BAC algorithm, with parameters $\lambda_1 = 0.15$, $\lambda_2 = 0.3$, $\lambda_3 = 0$. Here, λ_1 is set smaller than the previous bone examples due to the initialization, which must be updated more conservatively in order to avoid loops forming within the estimated contour. Figure 4.7 shows the final contour obtained from the same initial contour, where the only difference is which estimated pixel densities are used (i.e., corresponding to the outer or inner boundary). Note that both capture one of the intended boundaries. However, the contour is not able to split into two separate contours, in order to capture both the outer and inner boundaries simultaneously. This

Figure 4.7: Final segmented contour (in blue) for a binary, no-noise donut image using BAC (left two panels) and TOP+BAC (right). The two left contours are obtained from the same initial contour (red), with interior and exterior pixel densities based on the outer boundary (left) and inner boundary (right), i.e., $p_{\text{int}}^{(j)}$ and $p_{\text{ext}}^{(j)}$ for $j = 1$ (left) and $j = 2$ (right). The right set of contours is obtained after a topological initialization. BAC methods are performed using $\lambda_1 = 0.15$, $\lambda_2 = 0.3$, $\lambda_3 = 0$; TOP methods are performed using $\sigma_1 = 5$, $\sigma_2 = 5$, $T = 5$, and convergence requires 81, 35, and 18 full iterations, respectively, for convergence tolerance of 10^{-7} .



can be misleading from a segmentation perspective, and is a drawback to current active contour methods.

The right panel of Figure 4.7 shows the result of using a topological segmentation to initialize. We easily identify two boundary curves which correspond to the outer and inner boundaries of the donut. TOP+BAC then runs separate active contour algorithms simultaneously and independently, using their respective estimated pixel density functions (since the ground truth segmentations are also known to be comprised of inner and outer boundaries). As expected from the bone example, the topological initialization is quite close to the estimated boundary, which explains why the algorithm converges very quickly. The benefit of the proposed method is the ability to automatically identify the two boundaries, rather than simply specifying two separate initializations due to a priori knowledge about the topological structure of the donut. Table 2 shows performance measures applied to the final segmentation formed by the enclosed portion of the two estimated contours. Note that one can compute the elastic shape distance for the outer and inner contours separately. All measures are comparable to values which were seen in the bone example of Table 1, indicating that TOP+BAC has performed reasonably well.

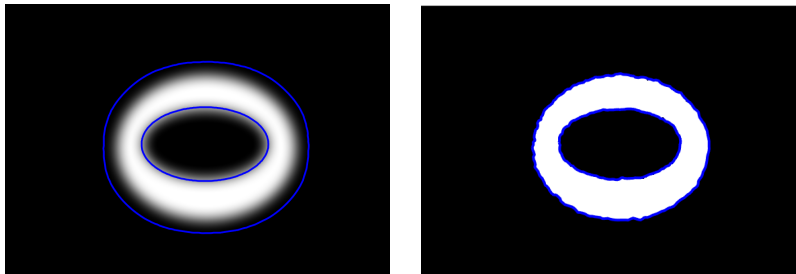
4.2.2 Binary Image with Noise

From the previous section, we have already seen the power of TOP+BAC for images with non-trivial topological features. To wrap up the simulation study, we also test performance of TOP+BAC on the types of artificial noise for which a topological initialization is feasible. In the study of the bone image, we found that Gaussian blur and Gaussian contour perturbations still allow for an easily interpretable estimated boundary from the topological mean-shift algorithm. Figure 4.8

Table 2: Performance metrics for TOP+BAC applied to donut with no noise (Figure 4.7), as well as the Gaussian blur and Gaussian contour perturbation examples (Figure 4.8). From top to bottom, measures are Hausdorff distance, Hamming distance, Jaccard distance, performance measure based on discovery rates, and the elastic shape distance for the outer and inner boundaries, respectively.

Measure	No noise	Blur	Perturbation
d_H	3.1623	9.0554	4.6904
p_H	0.0025	0.0822	0.0037
d_J	0.0185	0.3820	0.0243
PM	0.0194	0.4021	0.0259
Outer d_{Elastic}	0.0431	0.0586	0.1023
Inner d_{Elastic}	0.0799	0.0676	0.1578

Figure 4.8: Final segmented contour (in blue) for a donut image with Gaussian blur (left) and Gaussian contour perturbation (right) using TOP+BAC. Both images are segmented using a topological initialization to identify two boundary curves. BAC methods are performed using $\lambda_1 = 0.15$, $\lambda_2 = 0.3$, $\lambda_3 = 0$; TOP methods are performed using $\sigma_1 = 5, \sigma_2 = 5, T = 5$. Convergence requires 300 (the pre-specified maximum) and 24 full iterations, respectively, under convergence tolerance of 10^{-7} .



illustrates the two estimated boundaries under both of these types of noise. In both cases, two boundaries are easily identified from the topological initialization.

Interestingly, in the blurred donut image, the contours appear to expand slightly out past what one would expect to be the true contour; this is due to the use of the individually-estimated pixel density functions for each feature, in conjunction with the grayscale pixel values. This is reflected in the performance measures showed in Table 2. While the shape is close to the truth, the actual coverage as compared to true interior pixels is a bit off, which explains large values in the performance metric based on discovery rates, as well as the Jaccard index. The right panel of the same table shows similar results for a Gaussian perturbed contour. Note that shape distance is inflated due to the added Gaussian noise in the true boundary; many of the other measures are also inflated due to the added noise.

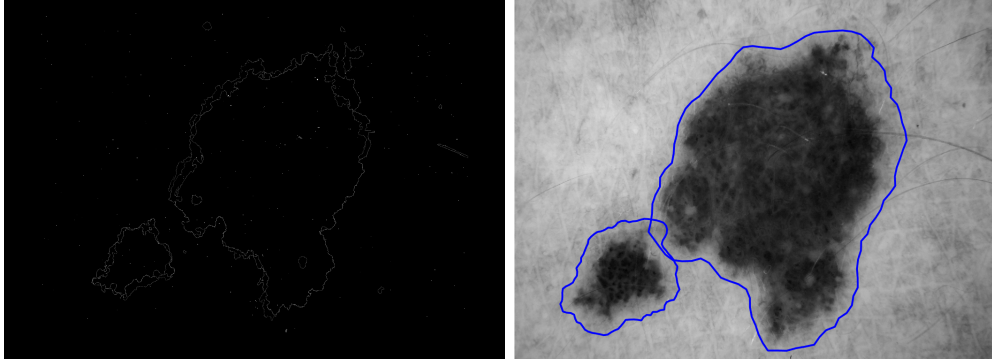
4.3 Real Data Evaluation

The method of TOP+BAC is not only applicable in topologically complex images, but also provides a powerful way to handle images with multiple objects. In order to demonstrate the benefit of our proposed method for images multiple objects, we conduct segmentation on a skin lesion dataset from Codella *et al.* (2018). The input data are dermoscopic lesion images in JPG format. The lesion images are taken from a historical sample of patients presented for skin cancer screening; these patients were reported to have a wide assortment of dermatoscopy types, from many anatomical sites. A subset of these images have ground truth segmentations, which were reviewed and accepted by a human expert. These ground truths are used to compute performance measures.

It is important to note that all of the “true” segmentations were identified as one connected component with no holes; however, there are many lesion images that consist of multiple well-defined connected components, thus making TOP+BAC beneficial for this task. We selected one image whose subject was diagnosed as a benign nevus lesion. This particular image, shown in Figure 4.9, appears to have two separate connected components corresponding to the lesion areas. In order to apply TOP+BAC, we require a training set of images to estimate interior and exterior pixel densities. To do this, we select nine other benign nevus skin lesion images with an identified ground truth segmentation. We note that these segmentations are marked as one connected component with no holes, leading to a mismatch with our suspected belief about the topological structure of the test image. To remedy this, we estimate just one set of pixel densities p_{int} and p_{ext} , as opposed to separate densities for each connected component. In addition, we use TOP to initialize BAC.

Figure 4.9 shows the result of TOP+BAC applied to this benign nevus lesion. The left panel shows the result of the topological mean-shift algorithm. Note that there are some extraneous boundaries, but the largest two coincide with the two separate connected components. One should note that while there are additional connected components in those regions, they are identified by MATLAB’s `bwboundaries` function as being contained inside the outermost boundaries, and thus, we are able to easily extract the two outer boundaries. If we initialize with these contours, and run two separate active contours using weights $\lambda_1 = 0.3$, $\lambda_2 = 0.3$, $\lambda_3 = 0$, we obtain the final segmentations on the right side of the figure after 300 iterations. We justify setting $\lambda_3 = 0$ by the quality of the ground truth, since some of the hand-drawn true segmentations are much coarser than others. In addition, shape registration can be challenging in the presence of noisy boundaries (since the SRVF is defined with respect to the time-derivative of the shape’s contour), which is the case with these skin lesions. Practically, it is of medical importance to identify whether a lesion consists of multiple smaller regions or one large region (Takahashi *et al.*, 2002). It is interesting to

Figure 4.9: Results of TOP+BAC on another benign nevus lesion image from the ISIC-1000 dataset. (Left) Boundary map obtained from TOP, used to initialize two active contours. (Right) Estimated final contours based on the topological initializations (TOP+BAC), using parameters $\lambda_1 = 0.3$, $\lambda_2 = 0.3$, $\lambda_3 = 0$ for BAC; parameters $\sigma_1 = 1$, $\sigma_2 = 5$, $T = 5$ for TOP.



note that while two connected components are easily identifiable visually from the image, the two active contours resulting from TOP+BAC in terms of physical distance are actually very close to each other due to the lack of separation.

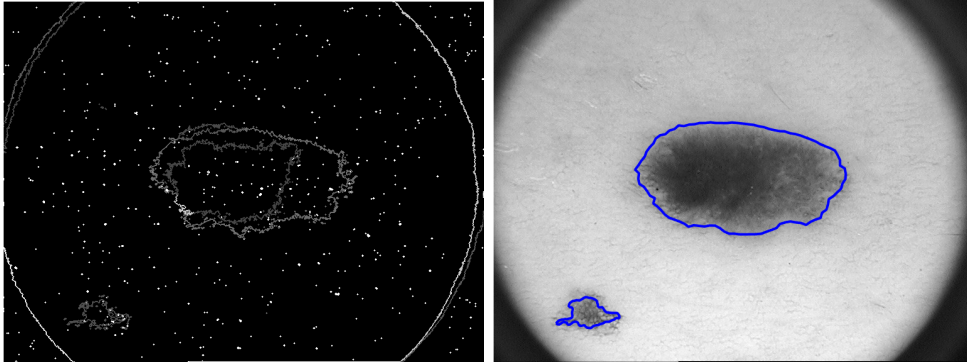
Figure 4.10 shows a second benign nevus image, again using nine training images to estimate pixel densities. Under the same settings as the other example in this section, we use TOP to initialize two active contours. In order to initialize around the two regions of interest, we can use TOP to cycle through connected components until we have selected two which are in the approximately correct regions. Then, BAC is performed using the same settings, with convergence requiring 114 steps. Note that in this case, the two regions are very well-separated, and thus, we do not run into the same phenomenon of close regions due to the gradient updates being applied separately for each contour. This is clearly a case in which a single active contour will not represent this lesion appropriately, whereas TOP may identify too many spurious boundaries which do not correspond to the actual target of interest (the rash).

5 Conclusion

5.1 Contribution

The motivation of this work is trying to combine two kinds of information (i.e. shape and topology) in image segmentation when they are both available. It also attempts to address the comment that “no effort was made to compare these (TDA) methods to simpler, more traditional statistical methods” by Wasserman (2018). In the first half of our paper, we briefly reviewed two different philosophies of image segmentation problem and outline TOP (treating segmentation as a cluster-

Figure 4.10: Results of TOP+BAC on a benign nevus lesion image from the ISIC-1000 dataset. (Left) Boundary map obtained from TOP, used to initialize two active contours. (Right) Estimated final contours based on the topological initializations (TOP+BAC), using parameters $\lambda_1 = 0.3$, $\lambda_2 = 0.3$, $\lambda_3 = 0$ for BAC; parameters $\sigma_1 = 1$, $\sigma_2 = 5$, $T = 5$ for TOP.



ing problem via mean-shift) and BAC (treating segmentation as a curve estimation problem) as representative methods for each. TOP (Paris & Durand, 2007) is a topologically-based method, which can also be used for clustering, while BAC (Joshi & Srivastava, 2009; Bryner *et al.*, 2013) is a method which combines traditional active contour segmentation approaches with shape analysis. We evaluated their performances, both qualitatively and quantitatively using various performance measures (Huang & Dom, 1995; Monteiro & Campilho, 2006; Arbelaez *et al.*, 2011). Based on this systematic study, we described their respective advantages and drawbacks in different scenarios and provided detailed suggestions.

In the second half of our paper, we propose a method that combines TOP and BAC. Both methods individually require parameter tuning, and more often than not, are very sensitive to this choice. TOP generally yields topologically consistent but overly conservative non-smooth contours and includes many noise regions. BAC is not necessarily “topologically aware”, but provides rather smooth contours and is not as sensitive to noise points, but highly dependent on the algorithm initialization. The proposed TOP+BAC method uses the segmentation result of TOP as an initialization of the BAC. This two-step method can be thought of as using BAC to “smooth-out” the result of TOP, with initial curves provided for each topological feature to allow for independent BAC algorithms to be run. We illustrate that topological information can be used to choose a good starting point of the gradient-descent algorithm. We supported our point that TOP+BAC is a better method by showing its performance using both artificial and real data. For artificial data, we illustrate that TOP+BAC can identify the complex topological structure of the image subject correctly, which enhances the interpretability of the segmentation result. For skin lesion diagnosis, TOP+BAC correctly identifies multiple objects (i.e., connected components) in the image, which can be of practical importance (Takahashi *et al.*, 2002).

5.2 Future Work

This work, as said above, is a primitive attempt to address the question asked by Wasserman (2018) in an image segmentation problem. There is a lot more to explore following the question discussed therein. One possible direction for future work is the problem of uncertainty quantification of estimated boundaries. To our knowledge, in the setting of multiple objects and single object with nontrivial topological features, not much work has been done concerning uncertainty quantification. One particular difficulty in this scenario is that uncertainty occurs both in how the boundary is estimated, as well as the topological properties of the boundary. For example, if we draw a confidence band surrounding the segmented contour of two discs, their confidence bands may intersect and create a single large connected component. BAC is extremely sensitive to numerical issues of gradient-descent when initialized poorly, so there are scenarios in which it will not converge at all, or creates fake loops on the boundary. Then, it is not straightforward to characterize this change of topological features when quantifying uncertainty. Another issue is that the BAC model (Bryner *et al.*, 2013) we used here is not a full Bayesian model, and therefore it is not obvious how to generalize this method to obtain a full posterior distribution for the segmentation. To address this issue, we believe that a general fully Bayesian model should be proposed and studied in the future.

Some interesting ideas arise from the segmentation of Figure 4.9. Note that TOP+BAC yielded two close contours which overlapped. This behavior occurs due to the estimated interior and estimated pixel densities from the training images where many of the true segmentations of the skin lesion images are somewhat distant from the portion of the lesion which is darkest. This may be due to human expert bias during segmentation. One may inherently be conservative when drawing a boundary surrounding the lesion, in an attempt to capture the entire lesion and avoid missing a key part of it. Since the active contour algorithm depends on the training data to estimate pixel densities, the final segmentation will also reflect this behavior. The expansion of the two contours to include lighter pixels is also partly due to the lack of a big separation between the two features. Gradient-descent updates are expected to be small if the two connected components are well-separated. Finally, the estimated pixel densities (using a ground truth segmentation which features just one connected component) reflect a primarily dark interior and light exterior.

Due to the lack of separation between features, a contour for one feature may attempt to include pixels from the other feature in order to match this density as best as possible. An alternate solution to this issue is to develop a conditional algorithm, i.e., use a topological segmentation to initialize the largest feature, and run active contours marginally on this feature. Once TOP is completed, one can then perform active contour updates on the next largest feature, constrained to the sub-region which removes the final contour from the first feature. This is left as future

work.

As already pointed out by Gao *et al.* (2013), there are other alternatives in TDA to handle topological information in a pixel image. In this paper, we pursue the TOP method by Paris & Durand (2007) which focuses on the pixel density estimator on grayscale images but can generalize to colored images. Currently, there is not any attempt to compare the performance and computational costs of different topological methods, or even a combination of two topological methods for a specific problems. The reason why a combination could be useful is that we can decide which topological method to use according to the signal-to-noise ratio in the image and the computational budget. We believe it is of great interest to carry out such a comprehensive study for topological methods in the image segmentation problem.

5.3 Acknowledgments

We would like to acknowledge and thank Yu-Min Chung for pointing out the skin lesion dataset to us. We would also liked to thank Sebastian Kurtek for his enthusiastic help and comments on the manuscript.

References

- Abdulrahman, Hasan, Magnier, Baptiste, & Montesinos, Philippe. 2017. From contours to ground truth: How to evaluate edge detectors by filtering. *Journal of WSCG*, **25**(2), 133–142.
- Arbelaez, Pablo, Maire, Michael, Fowlkes, Charless, & Malik, Jitendra. 2011. Contour Detection and Hierarchical Image Segmentation. *IEEE Trans. Pattern Anal. Mach. Intell.*, **33**(5), 898–916.
- Bai, Xiang, Yang, Xingwei, Jan Latecki, Longin, Liu, Wenyu, & Zhuowen, Tu. 2009. Learning context sensitive shape similarity by graph transduction. *IEEE Transactions in Pattern Analysis and Machine Intelligence*, **32**(5), 861–874.
- Bookstein, F. L. 1986. Size and Shape Spaces for Landmark Data in Two Dimensions. *Statistical Science*, **1**(2), 181–222.
- Bryner, Darshan, & Srivastava, Anuj. 2013. Shadow segmentation in SAS and SAR using Bayesian elastic contours. *Pages 375–380 of: Proceedings of the IEEE Conference on Computer Vision and Pattern Recognition Workshops*.
- Bryner, Darshan, & Srivastava, Anuj. 2014. Bayesian active contours with affine-invariant, elastic shape prior. *Pages 312–319 of: Proceedings of the IEEE Conference on Computer Vision and Pattern Recognition*.

- Bryner, Darshan, Srivastava, Anuj, & Huynh, Quyen. 2013. Elastic shapes models for improving segmentation of object boundaries in synthetic aperture sonar images. *Computer Vision and Image Understanding*, **117**(12), 1695–1710.
- Carlsson, Gunnar. 2009. Topology and data. *Bulletin of the American Mathematical Society*, **46.2**, 255–308.
- Caselles, Vicent, Kimmel, Ron, & Sapiro, Guillermo. 1997. Geodesic active contours. *International Journal of Computer Vision*, **22.1**, 61–79.
- Cheng, Yizong. 1995. Mean shift, mode seeking, and clustering. *IEEE Transactions on Pattern Analysis and Machine Intelligence*, **17**(8), 790–799.
- Codella, Noel CF, Gutman, David, Celebi, M Emre, Helba, Brian, Marchetti, Michael A, Dusza, Stephen W, Kalloo, Aadi, Liopyris, Konstantinos, Mishra, Nabin, Kittler, Harald, *et al.* 2018. Skin lesion analysis toward melanoma detection: A challenge at the 2017 international symposium on biomedical imaging (isbi), hosted by the international skin imaging collaboration (isic). *Pages 168–172 of: 2018 IEEE 15th International Symposium on Biomedical Imaging (ISBI 2018)*. IEEE.
- Dey, Tamal K., Sun, Jian, & Wang., Yusu. 2010. Approximating loops in a shortest homology basis from point data. *In: Proceedings of the Twenty-sixth Annual Symposium on Computational Geometry*. ACM.
- Dryden, I. L., & Mardia, K. V. 1992. Size and shape analysis of landmark data. *Biometrika*, **79**(1), 57–68.
- Dryden, I. L., & Mardia, K. V. 2016. *Statistical Shape Analysis: with Applications in R*. Second edn. New York: Wiley.
- Fasy, Brittany Terese, *et al.* 2014. Confidence sets for persistence diagrams. *The Annals of Statistics*, **42.6**, 2301–2339.
- Gameiro, Marcio, *et al.* 2015. A topological measurement of protein compressibility. *Japan Journal of Industrial and Applied Mathematics*, **32.1**, 1–17.
- Gao, Mingchen, *et al.* 2013. Segmenting the papillary muscles and the trabeculae from high resolution cardiac CT through restoration of topological handles. *In: International Conference on Information Processing in Medical Imaging*.
- Ghrist, Robert W. 2014. *Elementary applied topology*. Createspace.

- Hiraoka, Yasuaki, *et al.* 2016. Hierarchical structures of amorphous solids characterized by persistent homology. *Proceedings of the National Academy of Sciences*, **113.26**, 7035–7040.
- Huang, Qian, & Dom, Byron. 1995. Quantitative methods of evaluating image segmentation. *Pages 53–56 of: Proceedings., International Conference on Image Processing*, vol. 3. IEEE.
- Jaccard, Paul. 1901. Distribution de la flore alpine dans le bassin des Dranses et dans quelques régions voisines. *Bull Soc Vaudoise Sci Nat*, **37**, 241–272.
- Joshi, S. H., Klassen, E., Srivastava, A., & Jermyn, I. H. 2007. A Novel Representation for Riemannian Analysis of Elastic Curves in R^n . *Pages 1–7 of: Proceedings of the IEEE Conference on Computer Vision and Pattern Recognition*.
- Joshi, Shantanu, & Srivastava, Anuj. 2009. Intrinsic Bayesian active contours for extraction of object boundaries in images. *International Journal of Computer Vision*, **81(3)**, 331–355.
- Kass, M., Witkin, A., & Terzopoulos, D. 1988. Snakes: active contour models. *International Journal of Computer Vision*, **1**, 321–331.
- Kendall, D. G. 1984. Shape Manifolds, Procrustean Metrics, and Complex Projective Shapes. *Bulletin of London Mathematical Society*, **16**, 81–121.
- Kendall, David G. 1989. A survey of the statistical theory of shape. *Statistical Science*, 87–99.
- Klassen, E., Srivastava, A., Mio, W., & Joshi, S. H. 2004. Analysis of Planar Shapes Using Geodesic Paths on Shape Spaces. *IEEE Transactions on Pattern Analysis and Machine Intelligence*, **26(3)**, 372–383.
- Kurtek, S., Srivastava, A., Klassen, E., & Ding, Z. 2012. Statistical Modeling of Curves Using Shapes and Related Features. *Journal of the American Statistical Association*, **107(499)**, 1152–1165.
- Marques, Oge. 2011. *Practical image and video processing using MATLAB*. John Wiley & Sons.
- Monteiro, Fernando C, & Campilho, Aurélio C. 2006. Performance evaluation of image segmentation. *Pages 248–259 of: International Conference Image Analysis and Recognition*. Springer.
- Mumford, David, & Shah, Jayant. 1989. Optimal approximations by piecewise smooth functions and associated variational problems. *Communications on Pure and Applied Mathematics*, **42(5)**, 577–685.

- Paragios, Nikos, & Deriche, Rachid. 1999. Geodesic active regions for supervised texture segmentation. *Pages 926–932 of: Proceedings of the Seventh IEEE International Conference on Computer Vision*, vol. 2. IEEE.
- Paris, Sylvain, & Durand, Frédo. 2007. A topological approach to hierarchical segmentation using mean shift. *In: 2007 IEEE Conference on Computer Vision and Pattern Recognition*.
- Singh, Gurjeet, Mémoli, Facundo, & Carlsson, Gunnar E. 2007. Topological methods for the analysis of high dimensional data sets and 3d object recognition. *SPBG*.
- Small, C. G. 1996. *The Statistical Theory of Shape*. Springer.
- Späth, H. 1981. The minisum location problem for the Jaccard metric. *Operations-Research-Spektrum*, **3**(2), 91–94.
- Srivastava, A., Klassen, E., Joshi, S. H., & Jermyn, I. H. 2011. Shape Analysis of Elastic Curves in Euclidean Spaces. *IEEE Transactions on Pattern Analysis and Machine Intelligence*, **33**, 1415–1428.
- Srivastava, Anuj, & Klassen, Eric P. 2016. *Functional and Shape Data Analysis*. Springer-Verlag.
- Strait, J., Chkrebti, O., & Kurtek, S. 2019. Automatic Detection and Uncertainty Quantification of Landmarks on Elastic Curves. *Journal of the American Statistical Association*.
- Takahashi, K, Kobayashi, S, Matui, R, Yamaguchi, S, & Yamashita, K. 2002. The differences of clinical parameters between small multiple ischemic lesions and single lesion detected by diffusion-weighted MRI. *Acta neurologica scandinavica*, **106**(1), 24–29.
- Van de Weygaert, Rien, *et al.* 2011. *Transactions on Computational Science XIV*. Springer-Verlag. Chap. Alpha, betti and the megaparsec universe: on the topology of the cosmic web.
- Wasserman, Larry. 2018. Topological data analysis. *Annual Review of Statistics and Its Application*, **5**, 501–532.
- Wu, Pengxiang, *et al.* 2017. Optimal topological cycles and their application in cardiac trabeculae restoration. *In: International Conference on Information Processing in Medical Imaging*. Springer, Cham.
- Xia, Kelin, & Guo, Wei Wei. 2014. Persistent homology analysis of protein structure, flexibility, and folding. *International Journal for Numerical Methods in Biomedical Engineering*, **30.8**, 814–844.

- Younes, L. 1998. Computable elastic distance between shapes. *SIAM Journal of Applied Mathematics*, **58**(2), 565–586.
- Zahn, C. T., & Roskies, R. Z. 1972. Fourier Descriptors for Plane Closed Curves. *IEEE Transactions on Computers*, **21**(3), 269–281.
- Zhang, Yu Jin. 1996. A survey on evaluation methods for image segmentation. *Pattern Recognition*, **29**(8), 1335–1346.
- Zhu, Song Chun, & Yuille, Alan. 1996. Region competition: Unifying snakes, region growing, and Bayes/MDL for multiband image segmentation. *IEEE Transactions on Pattern Analysis & Machine Intelligence*, **9**, 884–900.